AIAA

A99-16318

AIAA-99-0426

LARGE EDDY SIMULATION OF SUPERSONIC BASE FLOW

C. Fureby[†], Y. Nilsson[†] & K. Andersson[‡]
FOA Defence Research Establishment
Dept of Weapons and Protection
[†]Div. of Warheads and Propulsion
[‡]Div. of Ballistics and EM Weapons
S-172 90 Stockholm
Sweden

37th AIAA Aerospace Sciences Meeting and Exhibit
January 11-14, 1999 / Reno, NV

LARGE EDDY SIMULATION OF SUPERSONIC BASE FLOW

C. Fureby[†], Y. Nilsson[†] & K. Andersson[‡]
[†]Dept. of Weapons and Protection, Div. of Warheads and Propulsion,
[‡]Dept. of Weapons and Protection, Div. of Ballistics and EM Weapons,
FOA Defence Research Establishment, S-172 90 Stockholm, Sweden

Abstract

Flow separation at the base of aerodynamic vehicles such as missiles, rockets and projectiles leads to the formation of a low-speed recirculation zone near the base. The pressure in this region is generally significantly lower than the freestream pressure, causing base drag which often is the dominant part of the total drag. The practical importance of increasing the understanding of axisymmetric base flows is the possibility of controlling the near-wake flow interactions so that base drag can be reduced at the same time as vehicle stability, control and overall performance can be enhanced. The ability to simulate the base region flow field as accurately as possible is therefore of major concern. In this study a computational capability based on a Large Eddy Simulation (LES) approach has been developed for predicting the flow around axisymmetric aerodynamic vehicles. In particular we have focused on turbulent supersonic base flow over a cylindrical afterbody, with and without base bleed, corresponding to laboratory experiments as to allow direct comparison with measurement data. Different subgrid models and spatial resolutions have been investigated for a case with zero base bleed, whilst further simulations with base bleed have been undertaken with the best performing subgrid model. Details of first and second order statistical quantities are presented and compared with experimental data. In general, good qualitative agreement is found whilst good quantitative agreement is reached only for the first order statistical moments, with the exception of the near wake region in which both good qualitative and quantitative agreement is achieved.

Introduction

Flow separation at the base of aerodynamic bodies of revolution with a blunt base, e.g. projectiles, rockets and missiles, leads to the formation of a low-speed recirculation region close downstream of the base. The pressure in this region, and thus on the base of the body, is generally significantly lower than the freestream pressure. This causes a base-drag force on the body which together with the pressure (or wave) drag (excluding the base) and the viscous drag constitutes the effective drag force. The base-drag component is a large part of the total drag and in experiments of axisymmetric bodies of revolution travelling at supersonic speeds, up to 35% to the drag is attributed to the base-drag, [1]. The pressure and viscous compo-

nents of drag cannot generally be considerably reduced without adversely affecting the stability of the aerodynamic body, and therefore recent attempts to reduce the total drag have been directed towards reducing the base-drag. A number of studies have been made to investigate the drag reduction due to the addition of a boattail, [2-4]. Although this is very effective in reducing the base-drag and thus the total drag, it is known to have negative impact on the aerodynamic stability, especially at transsonic speeds. Another effective way of reducing the base-drag is that of base-bleed or mass injection. Here, a small amount of mass is injected into the base region to increase the base pressure and thus reduce the base drag. This concept of base-bleed at the base has been carefully examined for supersonic flows, [4-8], while less data is available for transsonic flows, [9]. With the exception of [4, 9-11], reliable turbulence data in the base region is particularly scarce which presents a problem in validating simulation models. Thus, the practical importance of increasing the understanding of axisymmetric base flows is the possibility of controlling the near-wake flow interactions so that base drag can be reduced at the same time as vehicle stability, control and overall performance can be enhanced.

Supersonic base flows include several features that are quite formidable for accurate numerical simulations. Figure 1 is a schematic showing the important features of supersonic base flow with and without base-bleed. The supersonic freestream flow undergoes an expansion at the base corner as the turbulent approach boundary layer separates, and forms a free shear layer. This shear layer eventually undergoes recompression, realignment and redevelopment in the wake of the afterbody as it is constrained to turn along the axis of symmetry. The shear layer entrains fluid from the region after the base and subsequently accelerates it. The intense turbulent mixing and the energy exchange that characterise the free shear layer are important in determining the flowfield properties in the near-wake including the recirculation region. A recompression shock system returns fluid to the base region, forming a recirculation region in the process. Finally, the flow redevelops in the trailing wake. By adding a boattail to the cylindrical afterbody the initial conditions at the base-corner separation point change: this includes a higher freestream Mach number, non-zero local flow angle and non-zero pressure gradient due to the axisymmetric compression effect on the boattail as the flow approaches the axis of

1

symmetry. In addition, the presence of the boattail alters the state of the turbulent boundary layer by a rapid expansion at the body boattail junction and from the adverse pressure gradient acting on the boattail surface. Injection of cold, hot or combusting, [7-8], low-speed fluid into the near-wake translates the forward stagnation point downstream of the baseplane. The location of the forward stagnation point is determined by a balance between momentum of the injected fluid and that of the recirculating fluid.

Although experimental methods have given much insight into the behaviour of plane and axisymmetric base flow, at high Mach numbers experiments become increasingly difficult and expensive to perform. Furthermore, in some situations it is even necessary to extrapolate into regions inaccessible to present experimental facilities. With the rapid progress of high-performance computing, numerical methods, including Linear Stability Theory (LST) and Computational Fluid Dynamics (CFD) are becoming more widely used. Compressible plane wakes have been considered using LST by Gasperas, [12], who found that compressibility is stabilising. This was later confirmed by Chen at al, [13], who also concluded that the first non-linear structures to develop will always be two-dimensional. CFD simulations using the compressible Navier Stokes Equations (NSE) of supersonic base flow have been performed with Reynolds Averaged Simulation (RAS) models, [14-15]. In RAS, [16], all degrees of freedom smaller than the size of the largest energy containing eddies are averaged over to give equations for variables representing the mean flow. These are similar to the NSE but contain terms representing the effects of turbulent fluctuations on the mean flow; the modelling of these is the aim of turbulence modelling. These studies suggest that at least some RAS models perform reasonably well in predicting base pressure and mean velocity but are lacking in their predictions of the large-scale structures and the turbulence. In Direct Numerical Simulation (DNS) we attempt to solve the NSE exactly, i.e. the evolution of all eddy scales is considered. For supersonic base flow, DNS is impractical due to the large computational effort in resolving all scales of motion. Large Eddy Simulations (LES), [17-18], lies between the two extremes of DNS and RAS in cost, accuracy and resolution. In LES, a medium grid is used to simulate a system of modified NSE's in which eddy-scales smaller than the grid spacing are removed by low-pass filtering, whilst their effects on the resolvable or Grid Scale (GS) fluid dynamics is substituted by Sub Grid Scale (SGS) models. SGS models developed in physical or in adjoint space, [18-19], are introduced for closure and to provide a mechanism by which dissipation of kinetic energy accumulated at high wavenumbers can occur. A recent alternative, [20], involves solving the NSE with high-resolution monotone algorithms in which non-linear high-frequency filters are built into the nu-

merics providing implicit SGS models so that explicit SGS models can be dispensed with.

In the present contribution, LES is used to examine the spatio-temporal behaviour of supersonic base-flow with and without mass-injection. In particular the experimental configuration used in [9-11] is chosen as a natural compactly characterised test configuration. The aim of this investigation is to (i) analyse the predictive capabilities of compressible LES models based on either conventional LES models (using a simple eddy-viscosity SGS model) or Monotone Integrated LES models; (ii) examine the susceptibility of LES models to the specifics of explicit or implicit SGS models; (iii) study the physics of supersonic base-flow from aerodynamic bodies of revolution, with and without mass-injection; (iv) generate a database of first and second order statistical moments of the velocity for use in calibrating and improving conventional RAS models.

Formalism of Large Eddy Simulations

The fluid dynamic model used in the following study is based on the non-homogeneous compressible NSE, [21]. The working hypothesis in LES is the postulate that all dependent variables can be divided into GS and SGS components i.e. $f=\bar{f}+f'$. The resolvable GS components are defined by $\bar{f}=G*f$ where the kernel $G=G(x,\Delta)$ is any function of x and $\Delta=\Delta(x)$ endowed with the properties $\int_D G(x,\Delta)d^3x=1$, $\lim G(x,\Delta)=\delta(x)$ and $G(x,\Delta)\in C^n(\mathbb{R}^3)$ having compact support in the computational domain D with boundary ∂D and closure $D\cup\partial D$. The LES equations are obtained by convolving the NSE with G using the commutation relations $[\nabla,G*]f=(\frac{\partial G}{\partial \Delta}*f)grad\Delta+(Gfn)_{\partial D}$ and $[\partial_t,G*]f=0$, n being the outward pointing unit normal to ∂D, [22]. Following [22-23] it is evident that this lack of commutation induces additional terms in the LES equations, which thus become,

$$\begin{cases} \partial_t(\bar{\rho})+div(\bar{\rho}\tilde{v})=\mathfrak{S}^\rho(\bar{\rho},\tilde{v}), \\ \partial_t(\bar{\rho}\tilde{v})+div(\bar{\rho}\tilde{v}\otimes\tilde{v})=-grad\bar{p}+div(\overline{S}-B) \\ \qquad +\bar{\rho}\tilde{f}+\mathfrak{S}^v(\bar{\rho},\tilde{v}), \\ \partial_t(\bar{\rho}\tilde{E})+div(\bar{\rho}\tilde{v}\tilde{E})=div(\overline{h}-b)-\bar{p}div\tilde{v}+\pi+\overline{S}\cdot D \\ \qquad +\varepsilon+\bar{\rho}\tilde{\sigma}+\mathfrak{S}^E(\bar{\rho},\tilde{v},\tilde{E}), \end{cases} \tag{1}$$

where ρ is the density, v the velocity, p the pressure, $S=\eta trDI+2\mu D_D$ the viscous stress tensor, η the bulk viscosity, μ the kinematic viscosity, $D_D=D-\frac{1}{3}trDI$, $D=\frac{1}{2}(gradv+gradv^T)$, f the specific body force, $B=\bar{\rho}(\widetilde{v\otimes v}-\tilde{v}\otimes\tilde{v})$ the SGS stress tensor, E the specific internal energy, $h=\kappa gradE$ the heat-flux vector, κ the conductivity, $b=\bar{\rho}(\widetilde{Ev}-\tilde{E}\tilde{v})$ the SGS flux vector, $\varepsilon=\overline{S\cdot D}-\overline{S}\cdot D$ the SGS dissipation, $\pi=\overline{pdivv}-\bar{p}div\tilde{v}$ the SGS pressure-dilatation and σ the non-mechanical net-power. From the lack of commutation the terms $\mathfrak{S}^\rho(\bar{\rho},\tilde{v})$, $\mathfrak{S}^v(\bar{\rho},\tilde{v})$, $\mathfrak{S}^E(\bar{\rho},\tilde{v},\tilde{E})$ appear on the rhs of (1). Applying a Taylor series expansions in $\partial^k G/\partial\Delta^k$ an order of magnitude analysis shows that these are of

$O(\Delta^2)$ whilst the SGS terms are of $O(\Delta^{n-1})$ with $4/3 < n < 2$ – since $\mathbf{B}$ and $\mathbf{b}$ are of $O(\Delta^n)$.

Models for $\mathbf{B}$, $\mathbf{b}$, π and ε are required to complete the LES equations and to provide for the interaction between the large and small scale components. Following [17], $\mathbf{B}$ and $\mathbf{b}$ can be decomposed into Leonard terms, $\mathbf{L}$ and $\mathbf{l}$, which represent the interaction of resolved eddies to generate small scale turbulence; cross terms, $\mathbf{C}$ and $\mathbf{c}$, representing interactions between resolved and unresolved eddies and may thus transfer energy in either direction, but mainly towards the small scale eddies; and Reynolds terms, $\mathbf{R}$ and $\mathbf{r}$, representing interactions taking place between small scale eddies as it produces the necessary energy transfer from the large to the small scales. From mathematical analysis and physical considerations, [22-24], $\mathbf{B}$ and $\mathbf{b}$ are known to be Grammian tensors provided that $G=G(|x|,\Delta)$, i.e. $G \in SU(3)$, also implying that $\mathbf{B} \in Psym$, where Psym is the set of all positive symmetric definite tensors. Moreover, since $\mathbf{B}$ and $\mathbf{b}$ are frame indifferent, [23], they are isotropic functions in their arguments. The realizability conditions follow from the Grammian nature of $\mathbf{B}$ and the necessary and sufficient conditions for $\mathbf{B} \in Psym$ can be expressed in terms of the three principal invariants of $\mathbf{B}$; $\frac{1}{2}tr\mathbf{B} \geq 0$, $\frac{1}{2}[(tr\mathbf{B})^2 - tr(\mathbf{B}^2)] \geq 0$ and $det\mathbf{B} \geq 0$.

The most popular closure models for $\mathbf{B}$ and $\mathbf{b}$ are based on gradient hypotheses in which the SGS models assume the following bijective correlations: $\mathbf{B} = \frac{2}{3}(\bar{\rho}k - \mu_k div\tilde{v})\mathbf{I} - 2\mu_k \tilde{\mathbf{D}}_D$ and $\mathbf{b} = -\kappa_k grad\tilde{E}$, where k, μ_k and κ_k are the SGS kinetic energy, eddy-viscosity and diffusivity respectively which have to be modeled separately. For this purpose we have the well known Smagorinsky-type models, [17-18], in which $k = c_I \Delta^2 \|\tilde{\mathbf{D}}\|^2$, $\mu_k = c_D \bar{\rho}\Delta^2 \|\tilde{\mathbf{D}}\|$ and $\kappa_k = \frac{c_D}{Pr_T}\bar{\rho}\Delta^2 \|\tilde{\mathbf{D}}\|$, where Pr_T is the turbulent Prandtl number. Alternatively, one-equation models, [25-26], can be used, in which k is taken from a modelled balance equation so that $\mu_k = c_k \bar{\rho}\Delta\sqrt{k}$ and $\kappa_k = \frac{c_k}{Pr_T}\bar{\rho}\Delta\sqrt{k}$. The model coefficients can be determined from the assumption of isotropy and a $|k|^{-5/3}$ inertial subrange behaviour but this approach is questionable in transient situations or in the proximity of wall boundaries. This provides the motivation for dynamic eddy-viscosity models where an attempt is made to evaluate the model coefficients dynamically using local information of the flow, [27-29]. This procedure involves a second level of filtering having a width larger than the original filter width Δ. This class of models turn themselves of in laminar flows and produce the correct behaviour of the SGS stresses near solid walls thus precluding the need for ad-hoc damping functions, and do not exclude backscatter effects. A drawback of dynamic models is that the model coefficients could become rapidly varying functions is both space and time, sometimes leading to numerical instability. A recommend remedy, [18], is to average the nominators and denominators in the expressions for the model coefficients in time or over homogeneous directions, localised regions of space or along streamlines, [30]. Other closure models include the scale similarity model, [31], RNG-based models, [32], and structure function models, [18]. In addition, models for $\pi = \overline{pdiv\mathbf{v}} - \bar{p}div\tilde{v}$ are not extensively elaborated on while some recent attention has been paid to $\varepsilon = \overline{\mathbf{S} \cdot \mathbf{D}} - \bar{\mathbf{S}} \cdot \tilde{\mathbf{D}}$, [33].

The LES equations and the selected SGS model are discretized using an unstructured finite volume method so that $D \cup \partial D \to T_\Delta$ where T_Δ is a partition of $D \cup \partial D$ into sub-volumes Ω_P of characteristic size Δ having centroids at x_P and face-area centroids at x_f and satisfying $\cup_P(\Omega_P) = D \cup \partial D$ and $\cap_P(\Omega_P) = \emptyset$. By letting $f_P = \frac{1}{\delta V}\int_{\Omega_P} f dV$ represent the discrete approximation to the cell-average of f over the Pth cell, Gauss theorem can be used to obtain the spatially discretized LES equations which in turn are integrated in time using multi-step methods. More precisely,

$$
\begin{cases}
\sum_{i=1}^m \left(\alpha_i \bar{\rho}_P^{n+i} + \frac{\beta_i \Delta t}{dV_P}\sum_f [\bar{\rho}\tilde{v}\cdot dA]_f^{n+i} \right) = 0, \\
\sum_{i=1}^m \left(\alpha_i (\bar{\rho}\tilde{v})_P^{n+i} + \frac{\beta_i \Delta t}{dV_P}\sum_f [(\bar{\rho}\tilde{v}\cdot dA)\tilde{v} - (\bar{\mathbf{S}} - \mathbf{B})dA]_f^{n+i} \right. \\
\qquad \left. + \beta_i (\bar{\rho}\tilde{f})_P^{n+i} \Delta t \right) = -\beta_i (grad\bar{p})_P^{n+i}\Delta t, \qquad (2) \\
\sum_{i=1}^m \left(\alpha_i (\bar{\rho}\tilde{E})_P^{n+i} + \frac{\beta_i \Delta t}{dV_P}\sum_f [(\bar{\rho}\tilde{v}\cdot dA)\tilde{E} - (\bar{\mathbf{h}} - \mathbf{b})\cdot dA]_f^{n+i} \right. \\
\qquad \left. - \beta_i (\bar{p}div\tilde{v} + \pi + \bar{\mathbf{S}}\cdot\tilde{\mathbf{D}} + \varepsilon + \bar{\rho}\tilde{\sigma})_P \Delta t \right) = 0,
\end{cases}
$$

where α_i and β_i are parameters of the integration, Δt the time step, dV_P the volume of Ω_P and dA_f the face area vector of face f of Ω_P satisfying $\cup_f(|dA_f|) = \partial\Omega_P$ and $\cap_f(|dA_f|) = 0$. Let the flux functions $\hat{f}_f^C(\tilde{v};\mu)$ and $\hat{f}_f^C(\tilde{E};\mu)$ be approximations for the convective fluxes $f_f^C(\tilde{v}) = ((\tilde{v}\cdot dA)\tilde{v})_f$ and $f_f^C(\tilde{E}) = ((\tilde{v}\cdot dA)\tilde{E})_f$ respectively, and the flux functions $\hat{f}_f^D(\tilde{v};\mu)$ and $\hat{f}_f^D(\tilde{E};\mu)$ be approximations for the combined diffusive and SGS fluxes $f_f^D(\tilde{v}) = ((\bar{\mathbf{S}} - \mathbf{B})dA)_f$ and $f_f^D(\tilde{E}) = ((\bar{\mathbf{h}} - \mathbf{b})\cdot dA)_f$ respectively. Here, $\mu = \mu(P)$ represents a set of grid points in a neighborhood of P. The functional dependencies of the fluxes on the nodal values of the variables (i.e. the functional reconstruction) define the method. Since the SGS terms in the LES equations are of $O(\Delta^{n-1})$ and $\Delta = O(|d|)$, where $|d|$ is the characteristic grid spacing, the leading order truncation error of the modified LES equations are required to be of $O(|d|^{(n-1)+1})$ or it will impair the effects of the SGS models. Hence, the spatial discretization should be of second-order accuracy or higher. In this study, a first-order functional reconstruction scheme is used for the advective fluxes resulting in a centered second order accurate method. The inner gradients of $\hat{f}_f^D(\tilde{v};\mu)$ and $\hat{f}_f^D(\tilde{E};\mu)$ are approximated by second-order central differencing resulting in a centered second order accurate method. To decouple the pressure-velocity system, a Poisson equation, derived from the discretised versions of the continuity and momentum equations, is constructed for the pressure. The time integration is carried out using the second order accurate three-point backward method and the resulting discretised equations $\bar{U}_P^{n+m} = H(\bar{U}_P^{n+i};\mu, i \in [1,m])$ with $\bar{U} = [\bar{p}, \tilde{v}, \tilde{E}]^T$ are solved with a segregated approach leading to a Courant number restriction; a maximum Courant num-

ber of Co≈0.2 gives satisfactory numerical stability and temporal accuracy.

An important role in the vorticity dynamics of shear flows is played by the dynamics of slender tube-like regions of vorticity, [34-35]. When such regions are much thinner than the main flow scales, the details of the internal vortex structure may not be significant, thus the important features involve only the strengths and positions of the centerlines of such vortices. In such regimes, we can expect that methods which will handle vortices in a manner similar to that of shocks will provide an efficient computational framework. Furthermore, important vortex interaction mechanisms such as vortex merger or reconnection, occur on convective time scales shorter than the diffusive time scales, and are thus essentially inviscid; however, a minimal nominal viscosity is required to trigger vortex merger or reconnection processes which cannot occur in inviscid fluids. Such features of the high Re vorticity dynamics have been used as the rationale behind successful techniques for their simulation, [36-37], and to supply the rationale for Monotone Integrated LES (or MILES), [20, 39], in which the NSE are solved using high-resolution monotone methods with embedded discretization related low-pass filters and implicit SGS models resulting from the non-linear functional reconstruction of the convective terms. Hence, the discretized MILES equations are,

$$
\begin{cases}
\sum_{i=1}^{m}\left(\alpha_{i}\rho_{P}^{n+i}+\frac{\beta_{i}\Delta t}{dV_{P}}\sum_{f}[\rho v \cdot dA]_{f}^{n+i}\right)=0, \\
\sum_{i=1}^{m}\left(\alpha_{i}(\rho v)_{P}^{n+i}+\frac{\beta_{i}\Delta t}{dV_{P}}\sum_{f}[(\rho v \cdot dA)v-SdA]_{f}^{n+i} \\
\quad +\beta_{i}(\rho f)_{p}^{n+i}\Delta t\right)=-\beta_{i}(gradp)_{p}^{n+i}\Delta t, \\
\sum_{i=1}^{m}\left(\alpha_{i}(\rho E)_{P}^{n+i}+\frac{\beta_{i}\Delta t}{dV_{P}}\sum_{f}[(\rho v \cdot dA)E-h \cdot dA]_{f}^{n+i} \\
\quad -\beta_{i}(pdivv+S \cdot D+\rho\sigma)_{P}\Delta t\right)=0,
\end{cases}
\tag{3}
$$

The functional reconstruction of $\tilde{f}_{f}^{C}(v;\mu)$ and $\tilde{f}_{f}^{C}(E;\mu)$ is done by a flux-limiting method which attempts to hybridise a high-order convective flux-function $\tilde{f}_{f}^{H}(\Phi;\mu)$ that is well-behaved in smooth regions with a low-order dispersion-free convective flux-function $\tilde{f}_{f}^{L}(\Phi;\mu)$ using a non-linear flux-limiter Γ. Thus $\tilde{f}_{f}^{C}(\Phi;\mu)=\tilde{f}_{f}^{H}(\Phi;\mu)-(1-\Gamma(\Phi;\mu))[\tilde{f}_{f}^{H}(\Phi;\mu)-\tilde{f}_{f}^{L}(\Phi;\mu)]$, so that if Φ is smooth near Φ_{P} then Γ should be close to unity, while in the vicinity of a discontinuity we require Γ to be near zero. In MILES the concept of Flux Corrected Transport (FCT) of Boris & Book, [39], is used which attempts to incorporate as much as possible of the anti-diffusion $[\tilde{f}_{f}^{H}(\Phi;\mu)-\tilde{f}_{f}^{L}(\Phi;\mu)]$ without violating the physical principles of causality, positivity (when appropriate) and monotonicity. Here the high-order flux-function uses linear interpolation and the low-order flux-function uses first order upwinding. The flux-limiter used is $\Gamma=\frac{1}{2}[(1-\vartheta/\zeta)sgn(\vartheta-\zeta)+(\vartheta/\zeta)sgn\vartheta-sgn(\vartheta-1)]$, where ϑ is the normalised variable corresponding to the kinetic energy $\frac{1}{2}|v|^{2}$ and the parameter ζ is assigned a value of 0.1. Note that if $\zeta>0.5$ the limiter enforces a TVD conservative method. The functional reconstruction of $\tilde{f}_{f}^{D}(\Phi;\mu)$,

the handling of the pressure-velocity system in (3), and the solution of (3_{2}) and the resulting Poisson equation is the here same as for the LES model (2).

With the intent of comparing LES and MILES the modified equations, corresponding to (2_{2}) and (3_{2}), involving Taylor series expansions of the discretised equations, can be used; For LES,

$$
\begin{cases}
\partial_{t}(\bar{\rho})+div(\bar{\rho}\tilde{v})=\mathscr{S}^{\rho}(\bar{\rho},\tilde{v})+O(\Delta t^{3},|d|^{3}), \\
\partial_{t}(\bar{\rho}\tilde{v})+div(\bar{\rho}\tilde{v}\otimes\tilde{v})=-grad\bar{p}+div(\bar{S}-B) \\
\quad +\bar{\rho}\tilde{f}+\mathscr{S}^{v}(\bar{\rho},\tilde{v})+O(\Delta t^{3},|d|^{3}), \\
\partial_{t}(\bar{\rho}\tilde{E})+div(\bar{\rho}\tilde{v}\tilde{E})=div(\bar{h}-b)-\bar{p}div\tilde{v}+\pi+\bar{S}\cdot\tilde{D} \\
\quad +\varepsilon+\bar{\rho}\tilde{\sigma}+\mathscr{S}^{E}(\bar{\rho},\tilde{v},\tilde{E})+O(\Delta t^{3},|d|^{3}),
\end{cases}
\tag{4}
$$

where $\mathscr{S}^{f}=\sum_{k=[t,c,d]}\mathscr{S}_{k}^{f}=\frac{1}{3}\Delta t^{2}\partial_{t}^{3}(\bar{\rho}\tilde{v})+div([Ggrad\tilde{L}]^{*})+\mathscr{S}_{d}^{f}(\tilde{v})$ is the leading order-truncation error consisting of the sum of the errors from the temporal-, convection- and diffusion discretisation, with $\mathscr{S}_{d}^{f}$ being of $O(|d|^{2})$, the exact expression depending on the SGS model applied. Here, an asterisk denotes the symmetric part. Similarly for the MILES model,

$$
\begin{cases}
\partial_{t}(\rho)+div(\rho v)=\mathscr{S}^{\rho}(\rho,v)+O(\Delta t^{3},|d|^{3}), \\
\partial_{t}(\rho v)+div(\rho v\otimes v)=-gradp+div(S+B)+\rho f \\
\quad +\mathscr{S}^{v}(\rho,v)+O(\Delta t^{3},|d|^{3}), \\
\partial_{t}(\rho E)+div(\rho v E)=div(h+b)-pdivv+S \cdot D+ \\
\quad \rho\sigma+\mathscr{S}^{E}(\rho,v,E)+O(\Delta t^{3},|d|^{3}),
\end{cases}
\tag{5}
$$

where $\mathscr{S}^{f}=\sum_{k=[t,c,d]}\mathscr{S}_{k}^{f}$ is equivalent to the leading-order truncation errors of the conventional LES model (4). Following Grinstein & Fureby, [38], we have that $B=\rho(KL^{T}+LK^{T}+\beta^{2}Ld\otimes Ld)$ and $b=\rho KgradE$, where $L=gradv$, $K=\beta(v\otimes d)$ and $\beta=(1-\Gamma)sgnv$, are the leading-order truncation errors of the low-order functional reconstruction used in the flux-limiting. From these expressions it may be concluded that the convection discretisation used in MILES introduces tensor-valued eddy-viscosity-type models (i.e. implicit SGS models) that correspond to the explicit scalar-valued eddy-viscosity models used in ordinary LES and that the tensorial nature of these implicit SGS models may improve the modelling required in anisotropic non-equilibrium flows.

Description of Base Flow Cases Considered

The computational configuration adopted in this investigation is based on the experimental work by Dutton and co-workers, [9-11], carried out in the blowdown-type wind tunnel at the Gas Dynamics Laboratory at the University of Illinois at Urbana-Champain. In the experiments high-pressure air enters a stagnation chamber and passes through a screen honeycomb-screen flow-conditioning module. The air is expanded to a design Mach number of Ma≈2.5 in the test section using a converging diverging nozzle and exits through a conical diffuser and an exhaust duct to the atmosphere. A more detailed description of

the design of the wind tunnel is given by Herrin, [41]. The freestream velocity, pressure and temperature are $u_\infty=576$m/s, $p_\infty=515$kPa and $T_\infty=294$K, respectively for the zero base-bleed cases, and $u_\infty=576$ m/s, $p_\infty=471$kPa and $T_\infty=300$K, for the cases with base-bleed or mass injection depending on the value of the mass injection parameter $I=\dot{m}/\rho_\infty u_\infty A_b$, where $\dot{m}$ is the bleed mass flow rate, ρ_∞ the freestream density and A_b the base area. The cylindrical afterbody used in the experiments has a radius of $r_b=31.75$mm, and for the base bleed cases it is equipped with a $r_j=12.70$mm bleed orifice so that the area of the base bleed jet is 16% of the total base area. The freestream Reynolds numbers are about $Re=2.2 \cdot 10^6$.

The computational configuration and the boundary conditions were designed to resemble, as closely as possible, the experimental set up and consist of a circular cylinder having an outer radius of $10r_b$, and extending $4r_b$ upstream of the base and $16r_b$ downstream the base. Supersonic inflow conditions are imposed at the upstream end of the simulated test section, and for the base bleed orifice subsonic inflow conditions are imposed. Open boundary conditions using a wave transmissive condition, are imposed at the downstream end of the simulated test section, and in the cross-stream direction. Furthermore, no-slip adiabatic boundary conditions are imposed on the afterbody and on the base-plane. The flow field is initially set to the freestream conditions (u_∞, p_∞, T_∞) everywhere and is then advanced in time until initial transients have disappeared whereafter statistical sampling is initiated. The time evolution of the flow is closely monitored in terms of time-histories of velocity $\bar{v}$, velocity rms-fluctuations $\bar{v}_{rms}=\langle(\bar{v}-\langle\bar{v}\rangle)^2\rangle^{1/2}$, where $\langle \cdot \rangle$ denotes the time averaging operation, and pressure $\bar{p}$ to determine when the flow is fully developed. The statistical sampling (or time averaging) is performed over an additional time sequence of 10τ, where $\tau=u_\infty/20r_b$ is the typical flow through time. Simulations for different SGS models or bleed rates are restarted from previous simulations and thus require shorter time for initial transients to disappear. Different non-uniform Cartesian grids held fixed in time with $Co\approx0.2$, are used and use between $3.5 \cdot 10^5$ (grid 1, with a typical cell-size of 1.5Δ) and $1.2 \cdot 10^6$ (grid 2, with a typical cell-size of Δ) cells. All grids are clustered close to the afterbody and towards the base plane; the grid points in the normal direction are exponentially stretched away from the body, having a minimum grid spacing of $5 \cdot 10^{-5} r_b$ allowing for approximately two grid points within the laminar sublayer. See table 1 for additional details of the different simulations and grids to be discussed below.

Examination of the Influence of SGS Models

With the objective of examining the influence of particular SGS models on the time-averaged flow we first performed simulations of the I=0 case employing (i) the Smagorinsky model (SMG), with $c_I=0.0066$ and $c_D=0.0120$, as recommended by Erlebacher et al, [31]; (ii) the One Equation Model (OEEVM), with $c_k=0.07$ and $c_\varepsilon=1.05$, as recommended by Yoshizawa, [26]; and (iii) the MILES model previously described. These three simulations were performed on the coarse grid and started in sequence. For each simulation the statistical sampling, carried out over six flow through times, was started after most intermediate transients had passed. The experimental data of Dutton et al, [4, 9-11], are generally considered very reliable, extensive and well documented and thus lend themselves to detailed comparisons. Since the primary objective of this study is not to examine and document the detailed behaviour of different SGS models in supersonic base flow, but to demonstrate the applicability of LES and to examine the spatio-temporal behaviour of such flows, we limit this comparison to first and second order statistical moments in the near wake. An extended study focusing on SGS modelling will be the subject of a forthcoming investigation.

Figure 2 compares predictions from the three different SGS models on grid 1 and predictions from the MILES model on grids 1 and 2, for the zero base bleed case (I=0), in terms of the non-dimensionalized mean axial velocity component. Profiles of $\langle\bar{v}_1\rangle/u_\infty$ are presented at four positions in the reversed flow and redevelopment region. The experimental measurements predict that the recirculation region ends at $x_1/r_b\approx2.70$ and therefore the first profile at $x_1/r_b=2.52$ is located in the reverse flow direction and the remaining profiles at $x_1/r_b=2.83$, 3.46 and 4.72 are located in the redevelopment region. As indicated in figure 2 no significant differences are observed in the mean axial velocity distribution between the different grids and we therefore continue to use the coarse grid in the following numerical simulations. This choice is further corroborated by comparing global parameters as listed in table 1, and contour plots of the mean axial and radial velocity components at the centreplane of the wake. In the freestream flow ($r/R>1$) no differences between the various models were detected whilst within the wake some differences can be observed. In particular, we note that all models overpredict the width of the recirculation bubble in the reversed flow region (figure 2a), with MILES giving the least satisfactory correlation with experiments. In the redevelopment region at $x_1/r_b=2.83$ the Smagorinsky model agrees less favourably with measurement data than the other models. Further downstream in the redevelopment region all models correlate equally well with experimental data. Comparison of second order statistical moments show somewhat larger deviations from experiments. However to draw further conclusions on the relative performance of the models in-depth studies are required which are out of the scope in the present investigation.

Results – Statistical Comparison

Of particular interest is the accurate prediction of the base pressure, and thus, the base drag. In figure 3 we show the time-averaged (or mean) base pressure non-dimensionalized by the freestream pressure $\langle \overline{p} \rangle / p_\infty$ from predictions and experiments, [9], over the base. Here, $r/r_b=0$ corresponds to the centreline of symmetry while $r/r_b=1$ corresponds to the base corner. The mean base pressure distributions exhibit only small variations across the base, except for a slight increase near the base corners, being in good agreement with the experimental data. From experiments, [9], it is clear that the mean base pressure initially increases with base bleed rate I, peaks around I=0.0148, and then decreases as I is increased further. This response is corroborated by simulations carried out at I=0, I=0.0113, I=0.0148 and I=0.0226 predicting the same trend. However, the magnitude of the base pressure is systematically overpredicted by about 5%. This observation appears independent of the spatial resolution since simulations using the fine grid for I=0 did not improve predictions. At least for I=0 the choice of SGS models did not further affect the base pressure level. A potential source of divergence may be the difference in approach boundary-layer thickness between the experiments and the simulations; a thick boundary-layer is generally accepted to have a base pressure enhancing effect similar to that of base bleed. In the simulations the approach boundary-layer upstream of the base corner is found to have a thickness of about $\delta \approx 2$mm and the associated friction velocities vary monotonically with I between approximatively $u_\tau=18.6$m/s and 21.5m/s. In the measurements, [9-10], the approach boundary-layer thickness is between $\delta \approx 3.1$mm and 3.3mm so that the associated friction velocities are between $u_\tau=23.3$m/s and 24.4m/s depending on I.

Table 1 shows some representative global parameters for the different cases, grids and SGS turbulence models. The Ma and Re numbers (Ma=u_∞/c and Re=$u_\infty r_b/\nu$) are based on the freestream conditions and the radius of the base. The Strouhal number (i.e. the non-dimensionalized shedding frequency S=fr_b/u_∞) is determined from time histories of velocity, temperature and pressure at different points in the computational domain. The location of the maximum reverse velocity, its value, the rear stagnation point (defined by the closure of the recirculation region) and the forward stagnation point (defined as the point where the bleed jet flow and the reverse flow meet) are determined from the time-averaged (or mean) velocity field $\langle \overline{v} \rangle$. Furthermore, the cross-sectional average base pressure is obtained from averaging the mean base pressure over the base. In general, good agreement between simulations and experimental data for these global parameters are obtained, however no experimental data is available for the St number. From these global data it appears that the simulations overpredict the cross-sectional average base pressure with

about 5% and underpredict the average length of the recirculation region by about 5%.

Figure 4 shows the distribution of the axial velocity component $\langle \overline{v} \rangle_1$ along the centreline. For I=0 the predicted maximum reverse velocity (0.32u_∞ at $x_1/r_b \approx 1.45$) is found to be in good agreement with the experimental value (0.34u_∞ at $x_1/r_b \approx 1.52$) irrespectively of resolution and SGS models. The rear stagnation point at $x_1/r_b \approx 2.45$ is slightly shifted upstream as compared with the experimental data for which $x_1/r_b=2.65$, [9]. With increasing I, the bleed jet exit velocity increases causing a downstream shift of the forward stagnation point. With the obvious exception of the I=0 and I=0.0226 cases, the location of the rear stagnation point ($x_1/r_b \approx 3.10$) appears to be virtually independent of I, which is in qualitative agreement with the experimental data of $x_1/r_b \approx 3.20$. Accordingly, the observed downstream shift of the forward stagnation point with increasing bleed rate has the effect of decreasing the size of the recirculation region. The predicted maximum reverse velocity for the I=0.0113 and I=0.0148 cases are both in close agreement with the corresponding experimental values of $-0.17u_\infty$ and $-0.05u_\infty$, respectively. The position of the anticipated maximum reverse velocity occurs progressively downstream, its magnitude diminishing with increasing base bleed in the same manner as found in the experiments. Furthermore, simulations of the highest bleed rate (I=0.0226) case show no reverse flow, suggesting penetration of the bleed jet into the wake region, an observation which is in good agreement with the experimental data of Mathur & Dutton, [9]. In general, the predicted axial velocity distribution is in qualitative and quantitative agreement with the experimental data; however, some discrepancies are found for $x_1/r_b>4$. This may be related to the finite size of the computational domain and the weak (<5%) reflections resulting from the wave transmissive conditions employed at the outer boundaries.

Figures 5 and 6 show the rms-velocity fluctuations $\overline{v}_i^{rms}=\langle (\overline{v}_i-\langle \overline{v}_i \rangle)^2 \rangle^{1/2}$ on the centreline. For the I=0 case the axial rms-velocity fluctuations $\overline{v}_1^{rms}$ are in good qualitative accordance with the experiments, initially decreasing along the centerline but recovering at the rear stagnation point due to reattachment. However near the peak reverse velocity the simulations overpredict the axial rms-velocity fluctuation by almost 10%. For I=0.0113 and I=0.0148, reasonable agreement between the measured and simulated axial rms-velocity fluctuations can be observed, although the simulations overpredict $\overline{v}_1^{rms}$ far downstream. For these cases the axial rms-velocity fluctuations have two maxima; the first occurs at the forward stagnation point, whilst the second occurs at the rear stagnation point. The first peak is due to the change in flow direction from axial to radial when the bleed flow meet the reverse flow in the recirculation region, while the second peak results as a consequence of the closure of the recirculation region. The magnitude of the first peak seems to decay with increasing bleed

rate because of the limited influence of the diminishing recirculation zone whilst the magnitude of the second maximum is less well predicted by the simulations. For the highest bleed rate, I=0.0226, the bleed flow penetrates further into the wake thus explaining the low axial $\bar{v}_i^{rms}$ and radial $\bar{v}_r^{rms}$ rms-velocity fluctuations observed in figures 5 and 6, which are in good qualitative agreement with experimental data, although consistently overpredicting their magnitudes. The influence of the complex flow at the stagnation points is stronger in the axial direction and, thus the peaks in the axial rms-velocity fluctuations are more prominent than those in the radial rms-velocity fluctuations. The anisotropy of the rms-velocity fluctuations on the centreline is evident from the differences in the axial, radial and tangential (not shown) rms-velocity fluctuation profiles.

In figure 7 the turbulent kinetic energy $\frac{1}{2}|\bar{v}_i^{rms}|^2$ along the centreline is shown. The occurrence of peaks in $\frac{1}{2}|\bar{v}_i^{rms}|^2$ at the stagnation points, and similarly, the decreasing levels of $\frac{1}{2}|\bar{v}_i^{rms}|^2$ with increasing bleed rate are similar to those found for $\bar{v}_i^{rms}$. Good qualitative agreement with experimental observations, e.g. [9], in terms of dependence on the mass injection parameter I, and the overall shape of the profiles can be observed. However, the quantitative agreement is only satisfactory for I=0 and I=0.0113, whilst for I=0.0148 and I=0.0226, $\frac{1}{2}|\bar{v}_i^{rms}|^2$ is considerably overpredicted. Predictions for I=0 show differences in the vicinity of the maximum reverse velocity, as noted in both the axial and radial rms-velocity fluctuations. For the I=0.0113 case, good quantitative agreement up to $x_1/r_b \approx 3.0$ is obtained, however, further downstream $\frac{1}{2}|\bar{v}_i^{rms}|^2$ is overpredicted by about 10%. From figures 5 and 6 it seems that the individual contributions from the axial and radial rms-velocity fluctuations are equally important to the resulting $\frac{1}{2}|\bar{v}_i^{rms}|^2$ profiles. The reasons for the inconsistencies of $\bar{v}_i^{rms}$ and $\frac{1}{2}|\bar{v}_i^{rms}|^2$ along the centreline are not fully understood. However, two reasons are examined for I=0, i.e. the SGS model and the spatial resolution. As previously discussed, the limited choice of SGS models did not influence the mean velocity and the rms-velocity fluctuations. The generally unsatisfactory quantitative agreement with experimental data and the observed high degree of anisotropy warrants a further study of SGS models including dynamic models, e.g. [27], and SGS differential stress equation models, e.g. [41] , and will be the subject of a forthcoming study. A grid refinement study was also undertaken using a finer grid (grid 2 having the characteristic cell size Δ), which however provided only minor improvements of the results.

Contour plots of the mean axial and radial velocity components at the centerplane of the wake for the I=0, I=0.0148 and I=0.0226 cases are presented in figure 8. Independently of the value of I the initial portion of the free shear layer is characterised by high velocity gradients. The predicted velocity distribution is in good qualitative agreement with the experimental data of Mathur & Dutton, [42], of which the flowfield data for I=0 is presented in [9]. The spreading of the axial velocity gradients is indicative of the development of the shear layer prior to reattachment, and also to the wake development downstream. The axial velocity distribution in the free shear layer downstream of the base appears to be separated in an inner region and an outer region of which the former appears to diverge more rapidly towards the centreline. The distribution of SGS kinetic energy supports this division of the shear layer by predicting high turbulence intensities in the inner region and thus high mass entrainment. This feature is most apparent for the I=0 case (figure 8a) because of the absence of the base jet and the associated inner shear layer and mass entrainment in the near wake. As implied by figures 8a-c the inner layer finally overtakes the outer region and consumes most of the total shear layer width. These findings are in good accordance with the experimental measurements, e.g. [4, 9]. The shape of the mean-velocity defect, and the recovery of the mean axial velocity downstream of reattachment is dependent on the parameter I; along the centreline, the flow reaccelerates to sonic speed at about $x_1/r_b \approx 4.8$, 5.6 and 5.8, for I=0, I=0.0148 and I=0.0226, respectively which is in good agreement with data, [9].

The radial velocity component is considerably smaller than the axial velocity component, emphasising the dominance of the axial velocity in the near wake. The steep radial velocity gradient at the base corner marks the turning of the flow through the expansion fan, whilst the radial velocity gradient further downstream, occurring at the recompression region, marks the start of the trailing wake. As the outer, inviscid, flow approaches the axis of symmetry, the radial velocity component continues to increase in magnitude, due to the axisymmetric effect, to a peak value of about $0.24u_\infty$ for I=0 at approximately two base radii downstream, and $0.29u_\infty$ for I=0.0148 at around three base radii downstream. The value of I clearly affects the strength of the recompression waves; for I=0 a very strong recompression is observed in the simulations, whilst at higher values of I this weakens to almost expire at I=0.0226. The mean tangential velocity component is negligible in comparison with the mean radial velocity component for all cases, however, it was observed to be larger when I≠0 and in particular for the I=0.0226 case. For I=0 the mean radial velocity distribution shows the acceleration of low-speed fluid outward at the base as it becomes entrained into the shear layer near the base corner, a feature that can be responsible for the rising base pressure with increasing radius r. Compared to the I=0 case the I=0.0113 and I=0.0148 cases appear to have a declining shear layer growth with downstream distance from the base whilst the I=0.0226 case appears to have an increased shear layer growth. Due to the mass entrainment from the recirculation zone this affects the base pressure; lowest base pressure is found at I=0.0148, which is the case having

the most reduced shear layer growth, whilst the increased shear layer growth for the I=0.0226 case leads to a relative decrease in base pressure as compared with the optimal I=0.0148 case.

Figure 9 presents the distribution of $\frac{1}{2}|\bar{v}_i^{rms}|^2$ and the turbulent shear stresses $\tau_{1r}=\langle \bar{v}_1'\bar{v}_r'\rangle$ at the centreplane in the near wake for the I=0, I=0.0148 and I=0.0226 cases. From figures 5 and 6 the axial rms-velocity fluctuations are found to dominate the radial and tangential rms-velocity fluctuations in the central part of the wake, and hence the distributions of $\frac{1}{2}|\bar{v}_i^{rms}|^2$ (figures 9a-9c, for cases I=0, I=0.0148 and I=0.0226 respectively) are expected to behave similarly to the axial rms-velocity fluctuation. For I=0, $\frac{1}{2}|\bar{v}_i^{rms}|^2$ increases in the radial direction over the shear layer, from the relatively low freestream level, to attain a peak value in the shear layer, whilst concurrently growing in the axial direction after separation. The global peak value of $\frac{1}{2}|\bar{v}_i^{rms}|^2$ ($0.031u_\infty^2$) appears upstream of reattachment in the subsonic area and agrees well with the measured peak value of $0.035u_\infty^2$, cf. [9]. For I≠0, two shear layers arise, one between the bleed jet and the recirculation region and one between the freestream flow and the recirculation region, each associated with a $\frac{1}{2}|\bar{v}_i^{rms}|^2$ distribution. The peak value of $\frac{1}{2}|\bar{v}_i^{rms}|^2$ in the inner shear layer generally occurs just upstream of the maxima associated with the outer shear layer. Prior to reattachment, however, the maximum is reached and a subsequent decay to the lower and fairly constant values within the trailing wake results. At least for I=0 the predicted distribution of $\frac{1}{2}|\bar{v}_i^{rms}|^2$ is in good qualitative agreement with the experimental data, [9]. The reason for the low values of $\frac{1}{2}|\bar{v}_i^{rms}|^2$ in the trailing wake is conjectured to be the lack of turbulence production which is due to low mean velocity gradients. The anisotropy of the rms-velocity fluctuations must influence the subgrid flow, suggesting that advanced SGS models will be required to capture the dynamics of the smallest resolvable scales. This may be one explanation for the poor quantitative agreement between predicted and measured profiles of $\frac{1}{2}|\bar{v}_i^{rms}|^2$. By comparing the distribution of $\frac{1}{2}|\bar{v}_i^{rms}|^2$ between the various cases the influence of the bleed jet on the mean flow becomes evident. With base bleed the peak turbulent kinetic energy can be considerably diminished, resulting in a reduction of mass entrainment from the recirculation region. This in turn reduces the shear layer growth and subsequently increases the base pressure.

The turbulent axial-radial shear stress component $\tau_{1r}=\langle \bar{v}_1'\bar{v}_r'\rangle$, presented in figures 9d-9f, for cases I=0 I=0.0148 and I=0.0226, respectively, dominates over the axial-tangential shear stress $\tau_{1r}=\langle \bar{v}_1'\bar{v}_t'\rangle$, found negligible in comparison with τ_{1r} throughout the near-wake. Irrespectively of the value of I, the distribution of τ_{1r} is reasonably close to the distribution of $\frac{1}{2}|\bar{v}_i^{rms}|^2$, and in particular we may observe that the peak values of $\frac{1}{2}|\bar{v}_i^{rms}|^2$ and τ_{1r} coincide. At least for the case I=0 the predicted distribution of τ_{1r} is in reasonable qualitative agreement with the experimental

results, [9]. Further comparisons at I=0.0113 and I=0.0226 with the experimental data [42] corroborate the good qualitative agreement between the measurement data and the simulations independently of the value of the mass injection parameter I. By comparing the distribution of τ_{1r} between the different cases the influence of the bleed jet on the mean flow is further corroborated. The peak shear stress decreases with increasing value of I up to approximately I=0.0148 from which it again starts to increase concurrently as $\frac{1}{2}|\bar{v}_i^{rms}|^2$ increases. This affects the mass entrainment from the recirculation region, and in turn, the shear layer growth which appears to be directly related to the base pressure. Hence, a correct prediction of the second order statistical moments $\tau=\langle \bar{v}'\otimes\bar{v}'\rangle$ is vital for the accurate prediction and subsequent understanding of the mechanisms affecting the base pressure.

Results – Topological Characteristics

Figure 10 shows the instantaneous Ma number distribution at the centreplane overlaid by iso-surfaces of the streamwise vorticity component $\bar{\omega}_1=\frac{1}{2}curl\bar{v}\cdot e_1$ for the I=0, I=0.0148 and I=0.0226 cases. Independently of the value of I the flowfields are strongly three-dimensional and unsteady – the unsteadiness being reduced by increasing the base bleed, having the additional effects of weakening the corner expansion and the downstream recompression. At the base corners, the expansion fans can be recognized by the increase in Ma number followed by the gradual recompression in the freestream flow with a diminishing Ma number. At low bleed rates, near the base, the flow is generally reversed virtually out to the corner, however, at higher bleed rates the flow only becomes reversed in the annular region around the bleed jet and downstream of the bleed jet, depending on the bleed rate. The free annular shear layer is turbulent and viscous forming at the base corner and developing downstream to reattachment, whereupon it forms the far wake. The pressure gradient and the shear stress gradients in the shear layer are reduced as the shear layer matures when turbulent mixing develops, entraining ambient fluid from the freestream into the wake. Base bleed seems to narrow the annular shear layer, and move it further from the centreline of symmetry. In addition, base bleed seems to increase the mixing near the corners, leading to reduction of shear stresses, but by directing most of the injectant into the recirculation region, downstream mixing is not fully developed. Hence, base bleed appears to result in reduced vorticity in the recirculation region. The vorticity distribution is extremly complicated and strongly dependent on the bleed rate I; For I=0 the vorticity distribution is dominated by axial vortices produced in the annular shear layer downstream of the base corner and in the region of mean reattchment. These axial vortices are unstable and exhibit a shedding-like behaviour. For I≠0 the annular Kelvin-Helmholtz instability, along the jet border, yields high intensity vortex

8

structures mainly consisting of axisymmetric rings enclosing a region of intense axial vorticity. The axisymmetric vortex rings are short-lived and therefore only present in the near wake region and may occasionally alternate with helicoidal vortices.

Figure 11 shows instantaneous end-view images (similar to those obtained experimentally by Bourdon et al, [11], for the I=0 case) at typical cross-sections downstream of the base for the I=0 and I=0.0148 cases respectively. These cross sections were chosen to represent the flow in the free shear layer, close to the mean reattachment and in the developing wake respectively. For the I=0 case excellent qualitative agreement with the experimental visualisations is obtained close to the mean reattachment and in the developing wake. A detailed comparison of the experimental and predicted end-view images located in the free shear layer and close to the mean reattachment indicates that the spatial resolution in the simulations is inadequate to resolve the small turbulent structures in the annular shear layer. However, further downstream in the region of reattachment, large coherent structures, having a characteristic size of between $r_b/10$ and $r_b/5$ and being considerably larger than the spatial resolution Δ, are observed in both simulations and experiments. In the developing wake the large coherent structures seems to have a preferred orientation of approximately $\pm45°$ from the principal axis which coincides with experimental data. Considering these end-view images it seems that the development and evolution of the large coherent structures is a realistic prediction based on the low-pass filtered NSE. Turbulent structures with a characteristic size smaller than Δ are implicitly represented by the SGS stress tensor, or the SGS kinetic energy and viscosity, with the low-pass filtered NSE allowing for a continuous transfer between unresolved and resolved scales. This conjecture is supported by other computational results, e.g. the development of 'worm' vortices in forced homogeneous isotropic turbulence, [30, 43], or transitional free jets, [37], using different spatial resolutions ranging from DNS to LES. For the I≠0 cases the development of the flow in the reversed flow and redevelopment regions are very different as may be seen in figure 10. In the free shear layer region the bleed jet dominates the flow field, close to the mean reattachment, however, the differences are less apparent, while further downstream, in the developing wake significant differences emerge as a result of the different spatio-temporal flow, governed primarily by the interactions of the free shear layers, the bleed jet and the expansion and recompression waves.

Concluding Remarks

In this study a computational capability based on LES has been developed to investigate the spatio-temporal behaviour of axisymmetric supersonic base flow with and without base bleed. In order to investigate the influence of the SGS model on the time av-eraged or mean velocity field in the near-wake region simulations for a zero base bleed case (I=0) were carried out using different SGS models. Two simple but well-established explicit eddy-viscosity models, the Smagorinsky model and the one-equation eddy-viscosity model, were used together with a Monotone Integrated LES model (MILES), using an FCT-type convection discretisation, resulting in an implicit tensor valued eddy-viscosity model. The tensorial features of this non-linear implicit eddy-viscosity model permits the simultaneous treatment of grid and flow anisotropies, whilst guaranteeing positivity, causality and monotonicity of the large scale flow. Irrespectively of SGS model good qualitative and quantitative agreement for both first and second order statistical moments between predictions and experiments can be observed. This suggests that the resolvable flow is fairly independent of the intrinsic details of the SGS model as found elsewhere, e.g. [29-30, 38]. The most pronounced difference between predicted and experimental results is that the recirculation region is somewhat shorter in the simulations than in the experiments. A possible explanation to this difference, supported by the underprediction of the base pressure, may be the contrariety in approach boundary-layer thickness between experiments and simulations. Further studies are thus required to investigate the dependence of the approach boundary-layer thickness and the influence of other SGS models. Additional sources of error that will be examined in a forthcoming investigation is the size of the computational domain and the associated wave-transmissive far-field boundary conditions. Moreover, the possible implications of using more advanced SGS models, such as differential stress equation models or dynamic Smagorinsky-type models, will be discussed elsewhere.

The influence of mass injection or base bleed on the near wake flowfield and on the pressure distribution on the base is investigated next. Since no significant differences between the different SGS models investigated for I=0 could be observed, the MILES model was chosen for the remaining simulations. In addition to the I=0 case, three other cases characterised by I=0.0113, I=0.0148 and I=0.0226 are studied. Excellent agreement between predicted and measured pressure distributions, showing almost uniform radial mean pressure profiles across the base are observed. As observed in the experiments, the mean base pressure increases with increasing base bleed I to attain a peak value at about I=0.0148, to then decrease with further increase in I. Furthermore, good qualitative and reasonable quantitative agreement with experimental results for the first and second order statistical moments are obtained at the centreline for these cases. In particular, the trends associated with altering the value of the mass injection parameter I are well reproduced by the simulations. However, some significant discrepancies between predictions and experimental results are observed for both the axial and radial rms-velocity fluctuations near both the rear and

9

forward stagnation points. By examining the axial and radial velocity distributions at the centreplane it can be seen that an increase in bleed rate is accompanied by the decreasing size and intensity of the recirculation region (due to the downstream displacement of the forward stagnation point) and a posterior reduction in the peak axial and radial rms-velocity fluctuations at the forward stagnation point. Injection increases the base pressure and therefore reduces the mean base drag. Maximum base pressure occurs when freestream flow turning is minimised. Hence, peak base pressures are reached when the entrainment of freestream air into the wake is minimised.

Acknowledgements

References

[1] Rollstin L.; 1987, "Measurement of Inflight Base Pressure on an Artillery-Fired Projectile", AIAA Paper No. 87-2427.

[2] Addy A.L. & White R.A.; 1973, "Optimization of Drag Minimums Including Effects of Flow Separation" ASME Transactions: Journal of Engineering for Industry, **96**, p 360.

[3] Agrell J. & White R.A.; 1974, "An Experimental Investigation of Supersonic Axisymmetric Flow over Boattails Containing a Centered Propulsive Jet", FFA, TN AU-913.

[4] Herrin J.L. & Dutton C.J.; 1994, "Supersonic Near-wake Afterbody Boattailing Effects on Axisymmetric Bodies", J. Spacecrafts and Rockets, **31**, p 1021.

[5] Bowman J.E. & Clayden W.A.; 1967; "Cylindrical Afterbodies in Supersonic Flow with Gas Ejection", AIAA.J., **4**, p 1524.

[6] Sykes D.M.; 1970, "Cylindrical and Boattailed Afterbodies in Transonic Flows with Gas Ejection", AIAA.J., **8**, p 588.

[7] Andersson K., Gunners N.-E. & Hellgren R.; 1976, "Swedish Base Bleed – Increasing the Range of Artillery Projectiles through Base Flow", Propellants and Explosives, **1**, p 69.

[8] Gunners N.-E., Andersson K. & Hellgren R.; 1988, "Base-Bleed Systems for Gun Projectiles", Gun Propulsion Technology, Steifel L. (ed.), Progress in Astronautics and Aeronautics, **100**, p 27.

[9] Mathur T. & Dutton J.C.; 1996, "Base-Bleed Experiments with a Cylindrical Afterbody in Supersonic Flow", J. Spacecrafts and Rockets, **33**, p 30.

[10] Herrin J.L. & Dutton C.J.; 1994, "Supersonic Base Flow Experiments in the Near Wake of A Cylindrical Afterbody", AIAA.J., **32**, p 77.

[11] Bourdon C.J., Dutton J.C., Smith K.M. & Mathur T.; 1998, "Planar Visualisations of Large Scale Turbulent Structures in Axisymmetric Supersonic Base Flows", AIAA Paper No. 98- 0624.

[12] Gasperas G.; 1989, "Transition Prediction for Two-dimensional Viscous Supersonic Wakes", AIAA Paper No 89-0284.

[13] Chen J.H., Cantwell B.J. & Mansour N.N.; 1990, "The Effect of Mach Number on the Stability of a Plane Supersonic Wake", Phys. Fluids A 2, p 984.

[14] Chuang C.-C. & Chieng C.-C.; 1996, "Supersonic Base Flow Computation Using Higher Order Closure Turbulence Models", J. Spacecrafts & Rockets, **33**, p 374.

[15] Sahu J., Nietubicz C.J. & Steger J.L.; 1985, "Navier-Stokes Comptations of Projectile Base Flow with and without Mass Injection", AIAA.J. **23**, p 1348.

[16] Speziale C.G.; 1996, "Modeling of Turbulent Transport Equations", in Simulation and Modeling of Turbulent Flows Eds. Gatski T.B., Hussaini M.Y. & Lumeley J.L. Oxford University Press, New York.

[17] Rogallo R.S. & Moin P.; 1984, "Numerical Simulation of Turbulent Flows", Annu. Rev. Fluid Mech., **16**, p 99.

[18] Lesieur M. & Métais O.; 1996, "New Trends in Large Eddy Simulations of Turbulence", Annu. Rev. Fluid Mech., **28**, p 45.

[19] Galperin B. & Orszag S.A.; 1993, (Eds) "Large Eddy Simulation of Complex Engineering and Geophysical Flows", Cambridge University Press, Cambridge.

[20] Boris J.P., Grinstein F.F., Oran E.S., & Kolbe R.J.; "New Insights into Large Eddy Simulation", Fluid Dyn. Res., **10**, p 19.

[21] Lions P.L.; 1996, "Mathematical Topics in Fluid Mechanics", Oxford Science Publications, Oxford.

[22] Fureby C. & Tabor G.; 1997, "Mathematical and Physical Constraints of Large Eddy Simulations", J. Theor. and Comp. Fluid Dyn., **9**, p 85.

[23] Ghosal S, & Moin P.; 1995, "The Basic Equations for the Large Eddy Simulation of Turbulent Flows in Complex Geometry", J. Comp. Phys., **118**, p 24.

[24] Vreman B., Geurts B. & Kuerten H.; 1994, "Realizability Conditions for the Turbulent Stress Tensor in Large Eddy Simulation", J. Fluid Mech., **278**, p 351.

[25] Schumann U.; 1975, "Subgrid Scale Model for Finite Difference Simulation of Turbulent Flows in Plane Channels and Annuli", J. Comp. Phys., **18**, p 376.

[26] Yoshizawa A.; 1986, "Statistical Theory for Compressible Turbulent Shear Flow with the Application to Subgrid Modelling", Phys Fluids, A, **29**, p 2152.

[27] Germano M., Piomelli U., Moin P. & Cabot W.H.; 1994, "A Dynamic Sub Grid Scale Eddy Viscosity Model", Phys. Fluids A, 3, p 1760.

[28] El-Hady N.M. & Zang T.A.; 1995, "Large Eddy Simulation of Non-linear Evolution and Breakdown to Turbulence in High Speed Boundary Layers", Theor. and Comp. Fluid Dyn., 7, p 217.

[29] Kim W.-W. & Menon S.; 1994, "A New Dynamic One Equation Sub Grid Scale Model for Large Eddy Simu lations", AIAA Paper No 95-0356.

[30] Fureby C., Tabor G., Weller H. & Gosman, D.; 1997, "A Comparative Study of Sub Grid Scale Models in Homogeneous Isotropic Turbulence", Phys. Fluids., 9, p 1416.

[31] Erlebacher G., Hussaini M.Y., Speziale C.G. & Zang T.A.; 1992, "Toward the Large-Eddy Simulation of Compressible Turbulent Flows", J. Fluid Mech., 238, p 155.

[32] Yakhot V. & Orszag S.; 1986, "Renormalization Group (RNG) Methods for Turbulence Closure", J. Sci. Comp., 1, p 3.

[33] Vreman B., Geurts B., and Kuerten H., 1995, "Subgrid-Modelling in LES of Compressible Flow", Applied Sci. Res. 54, p 191.

[34] Jimenez J., Wray A., Saffman P., & Rogallo R.; 1993, "The Structure of Intense Vorticity in Isotropic Turbulence", J. Fluid Mech., 255, p 65.

[35] Porter D.H., Pouquet A., & Woodward P.R.; 1994, "Kolmogorov-like Spectra in Decaying Three-Dimensional Supersonic Flows", Phys. Fluids, 6, p 2133.

[36] Oberman E.A. & Zabusky N.J.; 1982, "Evolution and Merger of Isolated Vortex Structures", Phys. Fluids, 25, p 1297.

[37] Grinstein F.F.; 1995, "Self-Induced Vortex Ring Dynamics in Subsonic Rectangular Jets", Phys. Fluids, 7, p 2519.

[38] Fureby C. & Grinstein F.F.; 1998, "Monotonically Integrated Large Eddy Simulation of Free Shear Flows", AIAA Paper No 98-0537, accepted for publication in AIAA.J.

[39] Boris J.P. & Book D.L.; 1973, "Flux Corrected Transport I, SHASTA, a Fluid Transport Algorithm that Works", J. Comp. Phys. 11, p 38.

[40] Herrin J.L.; 1993, "An Experimental Investigation of Supersonic Axisymmetric Base Flow Including the Effects of Afterbody Boattailing", PhD Thesis, Univ. of Illinois at Urbana-Champaign, Urbana, IL.

[41] Fureby C., Tabor G., Weller H.G. & Gosman A.D.; 1997, "On Differential Sub Grid Scale Stress Models in Large Eddy Simulations", Phys. Fluids, 9, p 3578.

[42] Dutton C.J.; 1998, Personal Communication.

[43] Briscolini M. & Santangelo P.; 1994, "The Non-Gaussian Statistics of the Velocity Field in Low Resolution Large Eddy Simulations of Homogeneous Turbulence", J. Fluid Mech., 270, p 199.

I	Grid	SGS model	Ma	Re	St	λ_1/r_b	λ_2/r_b	$\langle\overline{p}\rangle/p_\infty$
0	Experimental data		2.46	$2.2 \cdot 10^6$	—	1.52	2.65	0.54
0	1, 350.000	Smagorinsky	2.42	$2.2 \cdot 10^6$	0.23	1.42	2.37	0.53
0	1, 350.000	One-equation	2.52	$2.4 \cdot 10^6$	0.19	1.47	2.44	0.51
0	1, 350.000	MILES	2.47	$2.3 \cdot 10^6$	0.21	1.45	2.45	0.52
0	2, 1.200.000	MILES	2.51	$2.3 \cdot 10^6$	0.24	1.50	2.67	0.51
0.0113	Experimental data		2.46	$2.2 \cdot 10^6$	——	2.40	3.20	0.65
0.0113	1, 350.000	MILES	2.53	$2.3 \cdot 10^6$	0.18	2.41	3.07	0.63
0.0148	Experimental data		2.46	$2.2 \cdot 10^6$	——	2.83	3.22	0.67
0.0148	1, 350.000	MILES	2.42	$2.2 \cdot 10^6$	0.19	2.83	3.14	0.68
0.0226	Experimental data		2.46	$2.2 \cdot 10^6$	——	—	—	0.64
0.0226	1, 350.000	MILES	2.48	$2.2 \cdot 10^6$	0.38	—	—	0.63

Table 1. Global statistics from experiments and simulations.
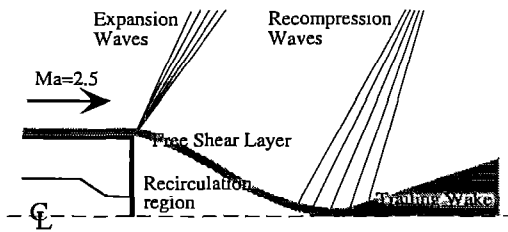
Figure 1. Schematic of the supersonic flow over an axisymmetric body of revolution.
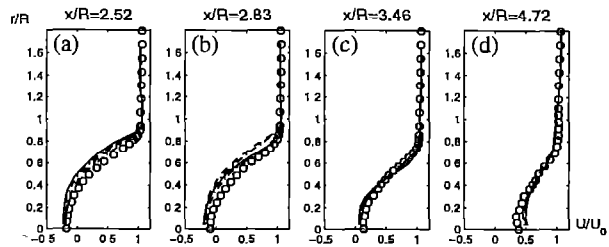
Figure 2. Comparison of velocity distributions in the wake for I=0 using different SGS models. Legend: (—) MILES, grid 1, (- - -) SMAG, grid 1, (- · -) OEEVM, grid 2, (······) MILES, grid 2 and (o) experiments.
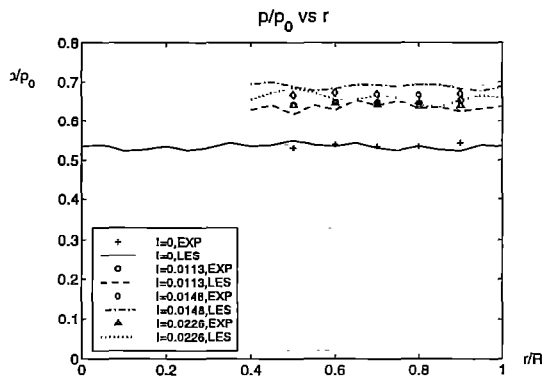

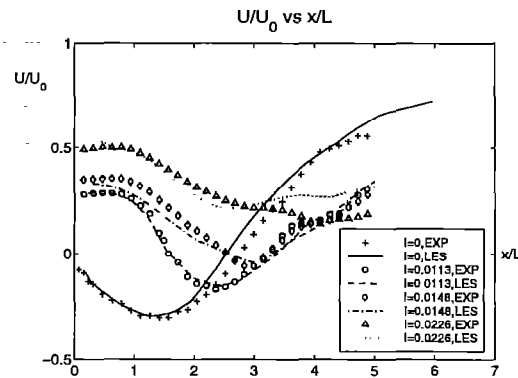**Figure 3.** Distribution of base pressure coefficient across the base.
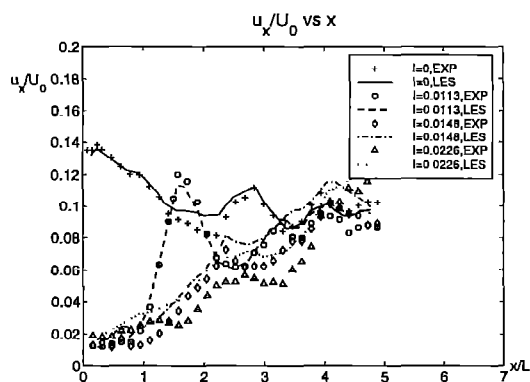

Figure 4. Mean axial velocity along the centerline.

Figure 5. Resolvable axial turbulence intensity along the centerline.
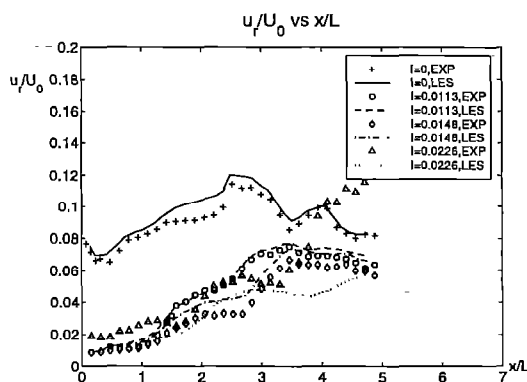
Figure 6. Resolvable radial turbulence intensity along the centerline.
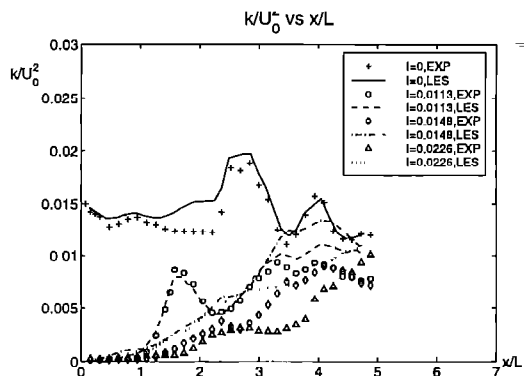
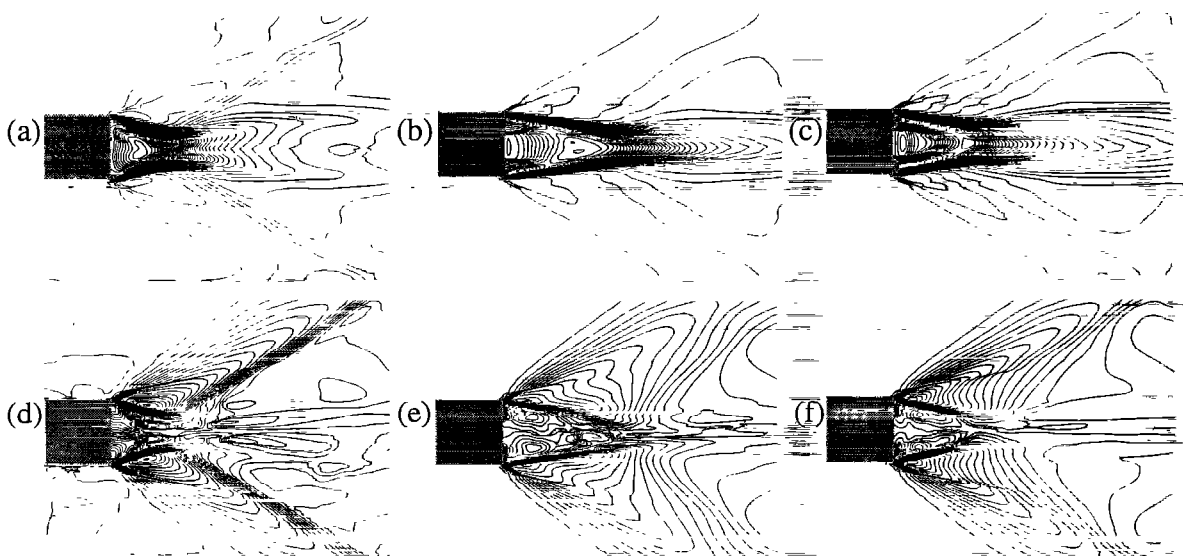**Figure 7.** Resolvable kinetic energy along the centerline.

Figure 8. Distribution of mean axial and radial velocity components at the centerplane for selected cases: (a), (d) I=0, (b), (e) I=0.0148 and (c), (f) I=0.0226.
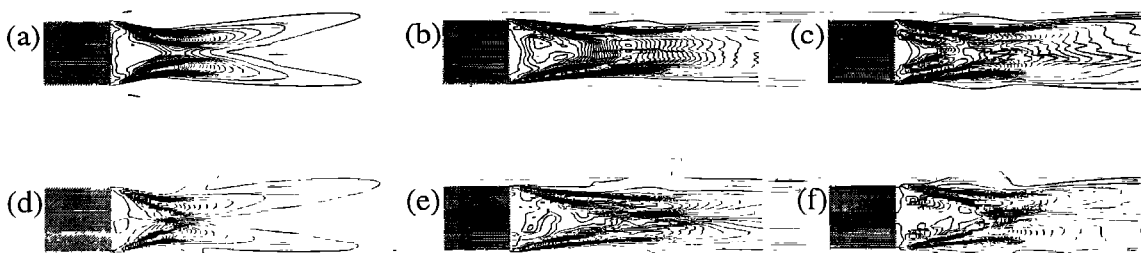

Figure 9. Distribution of resolvable kinetic energy and axial-radial turbulent shear stresses at the centerplane for selected cases: (a), (d) I=0, (b), (e) I=0.0148 and (c), (f) I=0.0226.
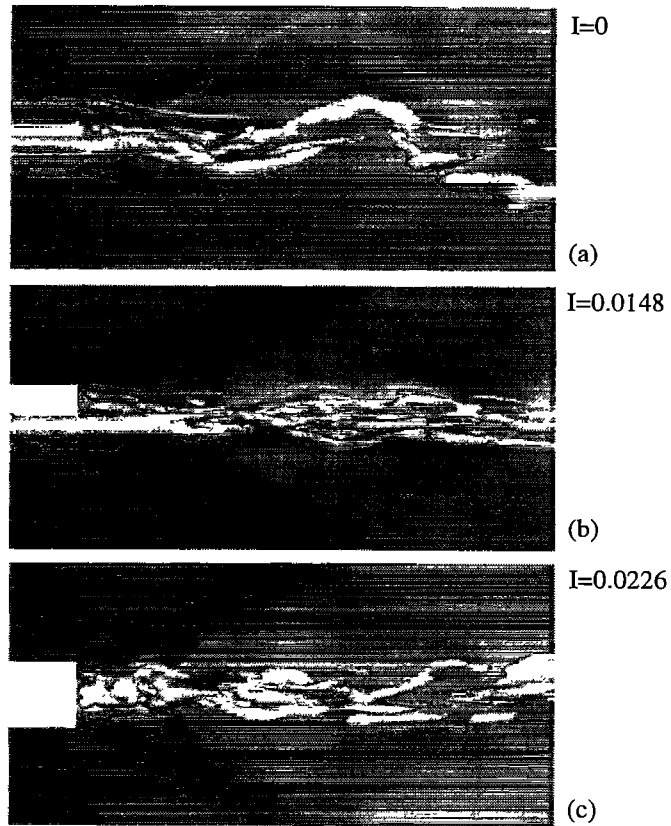
Figure 10. Instantaneous Ma number distribution at the centerplane superimposed by iso-surfaces of the streamwise vorticity component ω_1 for the I=0, I=0.0148 and I=0.0226 cases.
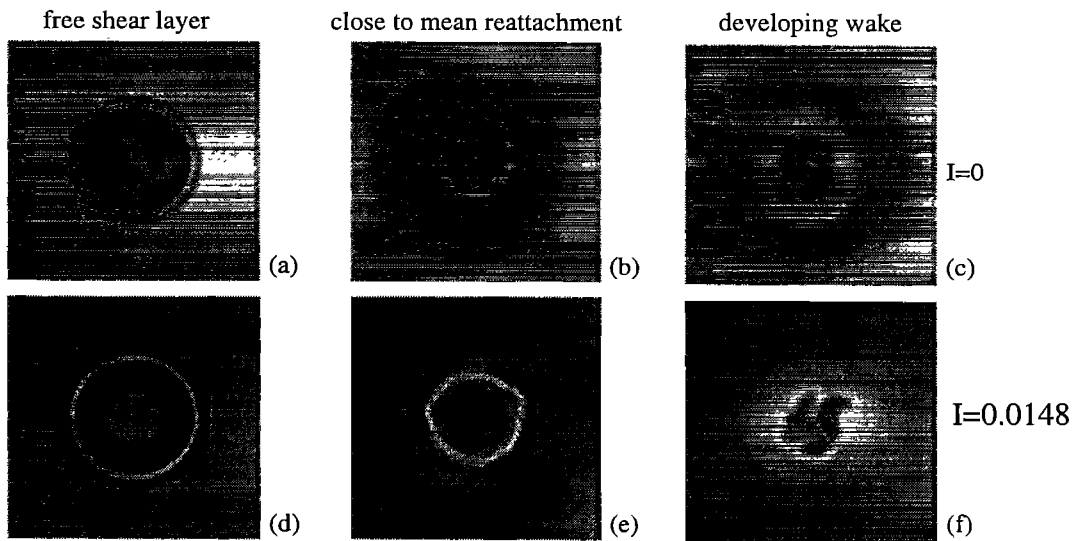

Figure 11. Instantaneous end-view images from I=0, I=0.0148 and I=0.0226.